A sparse reconstruction framework for Fourier-based plane wave imaging

Adrien Besson, Miaomiao Zhang, François Varray, Hervé Liebgott, Denis Friboulet, Yves Wiaux,
Jean-Philippe Thiran, Rafael E. Carrillo and Olivier Bernard

Abstract—**Ultrafast imaging based on plane-wave (PW) insonification is an active area of research due to its capability of reaching high frame rates. Among PW imaging methods, Fourier-based approaches have demonstrated to be competitive compared to traditional delay and sum methods. Motivated by the success of compressed sensing techniques in other Fourier imaging modalities, like magnetic resonance imaging, we propose a new sparse regularization framework to reconstruct high quality ultrasound images. The framework takes advantage of both the ability to formulate the imaging inverse problem in the Fourier domain and the sparsity of ultrasound images in a sparsifying domain. We show, by means of simulations, *in vitro* and *in vivo* data, that the proposed framework significantly reduces image artifacts, *i.e.* measurement noise and side lobes, compared to classical methods, leading to an increase of the image quality.**

Index Terms—**Ultrafast imaging, Fourier imaging, Sparse representation, ℓ_1-minimzation.**

I. INTRODUCTION

ULTRASOUND imaging (US) has become one of the most used imaging modalities in the last 30 years. In the conventional US systems, the number of transmitted waves is usually equal to the number of scan lines, thus limiting the frame rates to several tens of frames per seconds. Although this frame rate is sufficient to perform most of the applications of 2D US imaging, a higher frame rate is required for the understanding of more complex dynamics such as echocardiography for the heart motion analysis as well as for performing 3D or 4D imaging where thousands of scan lines are necessary. In order to address these challenges, synthetic aperture methods [1], [2] where few transducer elements are used to sequentially insonify the whole medium as well as methods based on plane-wave insonifications (PW) have thus been proposed. Methods based on PW transmissions use PW to insonify the whole medium with only few transmitted waves and backscattered echoes are processed in parallel to reconstruct many scan lines simultaneously. Using such modality, the frame rate is no longer limited by the number of scan lines but only by the

A. Besson, J.-Ph. Thiran and R. E. Carrillo are with the Signal Processing Laboratory (LTS5), Ecole polytechnique fédérale de Lausanne (EPFL), Lausanne, Switzerland.

A. Besson and Y. Wiaux are with the Institute of Sensors, Signals and Systems, Heriot-Watt University, Edinburgh, UK

O. Bernard, M. Zhang, F. Varray, H. Liebgott and D. Friboulet are with the University of Lyon, CREATIS, CNRS UMR5220, Inserm U1206, INSA-Lyon, University of Lyon 1, Villeurbanne, France. E-mail: olivier.bernard@creatis.insa-lyon.fr

J.-Ph. Thiran is with the Department of Radiology, University Hospital Center (CHUV) and University of Lausanne (UNIL), Lausanne, Switzerland.

time of flight of the US wave, allowing US imaging systems to reach thousands frames per seconds opening a whole range of applications such as shear wave elastography [3], imaging of pulse waves [4], ultrafast Doppler imaging [5], [6], ultrafast vector flow imaging [7] and imaging of contrast agents [8]. For an exhaustive presentation of the applications, one may refer to [9].

The development of ultrafast imaging has been intrinsically linked to the possibility to achieve efficient beamforming methods. When a PW reaches an inhomogeneity in the medium (scatterer), part of its energy is backscattered and the inhomogeneity becomes a secondary source. Assuming a propagation in a homogeneous medium with a given speed of sound, the propagation of the US wave from the secondary source back to the surface has an hyperbolic travel-time curve. The received echo signals thus consist in a set of hyperbolic curves coming from all the inhomogeneities in the medium and image reconstruction methods aim at inferring the position of the scatterers from these hyperbolic profiles. In order to do so, Montaldo *et al.* proposed a spatial-based approach in which the backscattered echo signals are integrated over all the possible hyperbolas. The value of the integral is then assigned to the corresponding point in the desired image [10]. Another approach has been proposed by Lu *et al.* in the 90s based on the use of limited diffraction beam theory to perform high frame rate imaging [11]–[14]. In their approach, a pulsed PW is used in transmission to reconstruct the Fourier spectrum of the desired image. They later extended their approach to various transmission schemes such as steered PWs (SPW) allowing an increase of the image quality [15]. Recently, Garcia *et al.* introduced an alternative to the method of Lu *et al.* based on a modification of the Stolt's f-k migration technique yielding image quality similar to the method of Lu *et al.* [16]. Recently, Bernard *et al.* proposed another alternative based on sampling the Fourier space radially and exploiting the Fourier slice theorem to retrieve the desired image spectrum, as in other imaging modalities such as computed tomography [17].

The use of ultrafast methods with only one PW leads to an image quality lower than conventional delay and sum (DAS) method with focus transmitted beams [18]. This decrease mainly comes from the fact that the transmitted energy, while spread in the entire medium, is far lower than when it is focused as in the conventional imaging configuration. To address this problem, coherent compounding of PWs has thus been introduced by Montaldo *et al.* [10]. Based on emitting -PW with well chosen angles and adding them with different delay strategies, this method enables creating a synthetic focus

in the full image range and leads to a noticeable increase of the image quality. However, PW compounding causes a decrease of the frame rate, proportional to the number of compounded PWs. Moreover, at large depth, this method becomes infeasible since the overlap of the PW does not cover homogeneously the distant regions relative to the probe size.

Compressed sensing (CS) has attracted much interest in the medical imaging community because of the potential to obtain high quality images from less data. By doing so, CS enables faster acquisition while guaranteeing similar image quality. The ability to apply CS framework to an imaging problem mainly relies on two pillars, namely the ability to relate the measurements to the desired image by a linear measurement process and the prior knowledge that images are sparse (or compressible) in a predefined model. Given these two pillars, it appears that medical imaging has characteristics that promote the use of CS. Firstly, the user can control the acquisition scheme in order to make it suitable to CS. Secondly, most of medical imaging modalities have measurement models which can be described by projections. In X-ray tomographic imaging (X-ray CT), the sinogram is related to the attenuation coefficient by the Beer-Lambert law (see [19] for detailed information) which, when discretized, leads to a linear system, thus compliant with the CS model. Moreover, gradient magnitude image sparsity is a powerful prior leading to an extensive number of applications of CS to X-ray CT based on total variation (TV) minimization [20]–[22]. In magnetic resonance imaging (MRI), k-space samples of the final image are acquired and the measurement model is an inverse discrete Fourier transform (FT). In their pioneer work, Lustig *et al.* proposed to retrieve the final image from partial Fourier data enforcing a sparsity prior both in the wavelet domain and under the TV transform [23] opening the way to fast MRI image acquisition. There has also been much work in applying CS reconstruction to more advanced MR techniques such as spread spectrum MRI [24], quantitative MR imaging [25], [26], diffusion MRI [27] and dynamic MRI [28], [29].

In the context of ultrasonic imaging, several studies have already exploited the sparsity of backscattered echo signals in the wave atom frame [30], as well as of radio frequency images in specific frames such as 2D Fourier basis [31], wavelet basis [32], or even learned dictionaries [33]. Schiffner *et al.* introduced CS-based plane wave beamforming in the frequency domain assuming sparsity in an orthonormal wavelet basis [34] while Chernyakova *et al.* used a Xampling scheme and a finite rate of innovation model to achieve CS-based Fourier beamforming [35]. In a recent paper, David *et al.* introduced CS-based time domain beamforming [36] in which the inverse scattering problem is solved using Green's function in an homogeneous medium.

Motivated by the success of CS for MR imaging, we introduce a sparse-based reconstruction of US images using Fourier-based beamforming methods. Indeed, insonifying a medium with a PW corresponds to populate the Fourier spectrum of the desired image with non-uniform Fourier samples [14], [16], [17]. Thus, as for MRI, Fourier-based beamforming methods aim at recovering an image from partial Fourier measurements coming from the spectrum of the backscattered echo signals. In order to apply a CS-based reconstruction, we formulate the imaging problem as a linear inverse problem relating the desired image to the spectrum of the echoes by a non-uniform Fourier transform (NUFT) [37]. Then we study several wavelet-based and Dirac-based models as sparsity priors.

The paper is organized as follows. In Section II, the CS framework is briefly summarized. Section III details the three existing Fourier-based reconstruction approaches in US imaging. In Section IV, the sparse reconstruction method is introduced. Section V describes the different experiments and simulations performed to evaluate the proposed methods. Experimental results of the evaluation are presented in Section VI and a discussion is followed in Section VII. Concluding remarks are given in Section VIII.

II. COMPRESSED SENSING FRAMEWORK

The now famous theory of CS introduces a signal acquisition framework that goes beyond the traditional Nyquist sampling paradigm [38]–[40]. Let $x \in \mathbb{C}^N$ be the signal under scrutiny. The fundamental premise in CS is that certain classes of signals, such as natural images, have a concise representation in terms of a sparsity dictionary Ψ, such that $x = \Psi\alpha$, where most of the coefficients α are zero, or small, and only few are significant. CS demonstrates that such sparse or compressible signals can be acquired using a small number of linear measurements and then recovered by solving a non-linear optimization problem [38]–[40].

Formally, the signal x is measured through the linear model $y = \Phi x + n$, where $y \in \mathbb{C}^M$ denotes the measurement vector, $\Phi \in \mathbb{C}^{M \times N}$, $M < N$, is the sensing matrix and $n \in \mathbb{C}^M$ represents the observation noise (or model inaccuracies). Recovering x from y poses an ill-posed linear inverse problem where the sparse prior on the signal regularizes the solution. CS shows that the following convex problem can recover x under certain conditions on the matrix Φ [41]:

$$\min_{\bar{x} \in \mathbb{C}^N} \|\Psi^\dagger \bar{x}\|_1 \text{ subject to } \|y - \Phi\bar{x}\|_2 \leq \epsilon, \qquad (1)$$

where $\Psi^\dagger$ denotes the adjoint operator of Ψ and ϵ is an upper bound on the ℓ_2-norm of the noise. Recall that the ℓ_p-norm of a complex-valued vector $a \in \mathbb{C}^M$ is defined as $\|a\|_p \equiv (\sum_{i=1}^{M} |a_i|^p)^{1/p}$, where $|\cdot|$ represents the modulus of a complex number. The choice of the ℓ_1-norm instead of the ℓ_0-norm (real measure of sparsity) is for convex relaxation purpose. See [40] for a thorough review on the mathematical principles of CS.

III. OVERVIEW OF THE FOURIER METHODS

When a PW is used to insonify a medium, the backscattered echo signals can be beamformed in the Fourier domain using Fourier-based beamforming methods [12], [16], [17] which share the same general scheme. The first step, called preprocessing, consists in applying a discrete 2D FT to the backscattered echo signals. The intermediate image obtained at this step is called preprocessed spectrum. The second step consists in relating the preprocessed spectrum to the desired

image by means of a NUFT, *i.e.* a FT on a non-uniform k-space defined by each method.

In the following sections, we will briefly summarize the different Fourier-based beamforming methods. As explained above, while the general scheme remains the same, the methods differ in the non-uniform space on which the NUFT is applied. Once this non-uniform space is defined, the desired image can be obtained from the preprocessed spectrum by taking the adjoint NUFT operator [37].
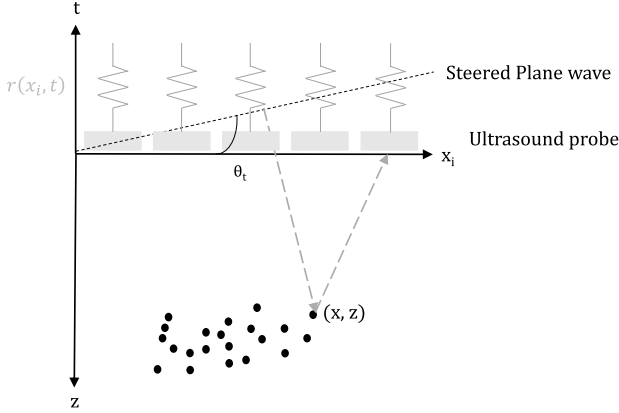

Fig. 1: Notations used in the remainder of the paper.

A. Lu method

Lu *et al.* derive X-waves relationship to theoretically model the behaviour of the transducers array in transmit and receive [14].

1) Preprocessing: The preprocessing step consists in taking the 2D FT of the backscattered echo signals. Formally, let us introduce $r(x_i, t)$ the backscattered echo signals. Then, the preprocessing is denoted as

$$y(k_x, k) = \iint_{x_i \in \mathbb{R}, t \in \mathbb{R}} r(x_i, t) e^{-j(k_x x_i + kt)} dx_i dt \quad (2)$$

$$= \mathcal{F}_{(k_x, k)}(r) \quad (3)$$

with $\mathcal{F}_{(k_x, k)}(.)$ the 2D FT on the frequency node (k_x, k) and $k = 2\pi \frac{f}{c}$, with f the temporal frequency.

2) Frequency remapping: In a pulse echo configuration, if we denote by (k'_x, k'_z), the k-space of the desired radio frequency (RF) image, the following relationship holds:

$$\begin{cases} k_x &= k'_x - k'_z \sin(\theta_t) = g_{x_L}(k'_x, k'_z) \\ k &= \frac{k'^2_x + k'^2_z}{2k'_z \cos(\theta_t) + 2k'_x \sin(\theta_t)} = g_{z_L}(k'_x, k'_z), \end{cases} \quad (4)$$

where (k_x, k) accounts for the k-space of the backscattered echo signals.

Thus, the final RF image $s(x, z)$ is related to the preprocessed spectrum by a NUFT on (k_x, k) defined by the remapping (4) and the following relationship holds:

$$y(k_x, k) = \mathcal{F}_{(g_{x_L}(k'_x, k'_z), g_{z_L}(k'_x, k'_z))} \{s(x, z)\}. \quad (5)$$

B. Garcia method

Garcia *et al.* propose a different approach for PW imaging based on Stolt's migration technique [16]. The main assumption is called exploding reflector model (ERM) and states that the scatterers in the medium all explode at the same time and become emitting sources. Considering the ERM wave field coming from a PW with angle θ_t, the objective is to retrieve the value of the field at $t = 0$ knowing the value of the field at the surface. Garcia *et al.* demonstrate that, as for Lu method, the 2D FT of the backscattered echo signals is linked to the 2D FT of the desired RF image by the remapping defined below.

1) Preprocessing: The preprocessing step, just like in Lu's method, consists in taking the 2D FT of the backscattered echo signals and the preprocessed spectrum $y(k_x, k)$ is given by (2).

2) Frequency remapping: The following relationship holds between the k-space representation of the desired RF image at (k'_x, k'_z) and the preprocessed spectrum:

$$\begin{cases} k_x &= k'_x = g_{x_G}(k'_x, k'_z) \\ k &= \frac{\hat{c}}{c} sign(k'_z) \sqrt{k'^2_z + k'^2_x} = g_{z_G}(k'_x, k'_z) \end{cases} \quad (6)$$

with $\hat{c} = \frac{c}{\sqrt{1 + cos(\theta_t) + sin^2(\theta_t)}}$.

The RF image $s(x, z)$ is related to the preprocessed spectrum by applying a NUFT on the k-space defined in equation (6) and we have the following relationship:

$$y(k_x, k) = \mathcal{F}_{(g_{x_G}(k'_x, k'_z), g_{z_G}(k'_x, k'_z))} \{s(x, z)\}. \quad (7)$$

with $g_{x_G}(k'_x, k'_z)$ and $g_{z_G}(k'_x, k'_z)$ defined in (6).

C. Ultrasound Fourier slice theory

Bernard *et al.* demonstrate, using the Fourier slice theorem, that the temporal FT of a received PW steered with a given angle is a radial line in the k-space of the desired image [17]. Thus, by simulating several steering angles θ_r at reception for a given angle at emission, it is possible to populate the spectrum of the desired RF image to recover it.

1) Preprocessing: The preprocessing step is slightly different than the two other methods and consists in three main steps for each steered angle θ_r [42]:

1. Apply a linear delay law P_{θ_r} on the backscattered echo signals: $y_1(x_i, t, \theta_r) = P_{\theta_r} \{r(x_i, t)\}$.
2. Sum the resulting signals on the lateral direction: $y_2(z, \theta_r) = \sum_{x_i} y_1(x_i, t, \theta_r)$.
3. Compute the 1D temporal FT of the resulting signal: $y(k, \theta_r) = \mathcal{F}_k(y_2)$ with $k = \frac{f}{c}$.

2) Frequency remapping: Given the preprocessed spectrum $y(k, \theta_r)$ defined in III-C1 and a steering angle θ_t at transmission, Bernard *et al.* show that the following relationship holds:

$$\begin{cases} k &= \frac{k'^2_x + k'^2_z}{2(k'_x \sin(\theta_t) + k'_z \cos(\theta_t))} \\ \theta_r &= \arctan\left(\frac{2k'_x k'_z \cos(\theta_t) + (k'^2_x - k'^2_z) \sin(\theta_t)}{2k'_x k'_z \sin(\theta_t) + (k'^2_z - k'^2_x) \cos(\theta_t)}\right) \end{cases}. \quad (8)$$

The region of the spectrum corresponding to a fixed value of θ_r is a line of angle $\xi_r = f_{\theta_t}(\theta_r)$ with $f_{\theta_t}(.) = \arctan((sin(\theta_t) + sin(.))/(cos(\theta_t) + cos(.)))$. Thus, for a

range of values of θ_r, the spectrum of the desired image is populated with lines of different angles. In the same way as Lu and Garcia methods, the final image is then related to the preprocessed spectrum by a NUFT on $(g_{x_B}(k'_x, k'_z) = k\sin\theta_r, g_{z_B}(k'_x, k'_z) = k\cos\theta_r)$ with k and θ_r given by (8). We thus have:

$$y(k_x, k) = \mathcal{F}_{(g_{x_B}(k'_x, k'_z), g_{z_B}(k'_x, k'_z))}\{s(x, z)\}. \qquad (9)$$

D. Image reconstruction

Given the relationship between the desired RF image $s(x, z)$ and the preprocessed spectrum $y(k_x, k)$, the classical way to retrieve the image from the preprocessed spectrum consists in performing an inverse NUFT. However, $y(k_x, k)$ does not have complete information on the spectrum of $s(x, z)$ thus recovering s from y is an ill-posed problem as it will be described in the following section. In classical beamforming approaches, the inverse NUFT is approximated by the adjoint NUFT, also known as the filtered back projection method, inducing measurement inaccuracies and image artifacts.

IV. SPARSE-BASED BEAMFORMING

A. Motivation

1) Fourier-based beamforming is an ill-posed problem: When a wave is emitted from a source with limited aperture, Lu has demonstrated that it generates so-called limited diffraction array beams [13]. Plane waves have been described as part of these limited diffraction array beams [13]. It has also been demonstrated that the k-space of the backscattered echo signals corresponding to plane wave insonification is limited by evanescence properties of the waves [14]. In the particular case of a plane wave with normal incidence, it may be ascertained that $k \geq |k_x|$ [15] with k_x a function of the aperture size. The k-space of the backscattered echo signals is then related to the k-space of the desired image through the remapping described in Section III. Thus, due to the evanescence properties, only part of the desired image k-space may be recovered as illustrated in Fig. 2 in [15]. Since the entire image spectrum cannot be retrieved, the problem is stated as ill-posed.

2) Interpolation schemes in the NUFT: Since the fast Fourier transform (FFT) algorithm cannot be applied on non-uniform grids, NUFT implies an interpolation process during the frequency remapping, in which the non-uniform space is projected on a uniform grid. This interpolation may create artifacts and loss of signals [37]. Usual ways to address this problem consists of zero-padding strategies or optimized interpolation schemes [37]. However, it implies a non-negligible additional computational cost and the quality improvement remains limited.

3) The proposed approach: The idea behind the proposed approach is to come up with an alternative to classical approaches in which the ill-posed problem is regularized by exploiting sparsity of the US images in an appropriate model. The desired image is then retrieved by solving a problem similar to (1).

B. Proposed sparse-based beamforming method

Since the method is based on the CS framework described in Section II, it relies on two pillars:

- The ability to pose the Fourier-based beamforming as an inverse problem.
- The sparsity of the ultrasound images in an appropriate model.

1) Problem formulation: The first pillar of the proposed method consists in deriving a measurement operator from the acquisition model. Formally, if $\mathbf{y}$ denotes the discretized preprocessed spectrum defined in Section III for the different methods, and $\mathbf{s}$ denotes the desired image, the objective is to identify Φ such that $\mathbf{y} = \Phi\mathbf{s} + \mathbf{n}$, where $\mathbf{n}$ accounts for noise and model perturbations.

2) Measurement operator: Notice that $\mathbf{s}$ is related to $\mathbf{y}$ by a 2D FT on a non-uniform space defined by the different remappings described in Section III.

Let us first consider the discretization of the preprocessing step. We define a regular grid for the backscattered echo signals, denoted as $\mathbf{r}$, and the corresponding k-space grid in the following equations:

$$\begin{cases} \boldsymbol{x_i} &= \left\{jp, \ \forall j \in \left\{\frac{-N_t}{2}, ..., \frac{N_t}{2} - 1\right\}\right\} \\ \boldsymbol{t} &= \left\{\frac{l}{f_s}, \ \forall l \in \{0, ..., N_r - 1\}\right\} \end{cases} \qquad (10)$$

and

$$\begin{cases} \boldsymbol{k_x} &= \left\{\frac{2\pi m}{p \times N_t}, \ \forall m \in \left\{\frac{-N_t}{2}, ..., \frac{N_t}{2} - 1\right\}\right\} \\ \boldsymbol{k} &= \left\{\frac{2\pi l f_s}{c \times N_r}, \ \forall l \in \{0, ..., N_r - 1\}\right\} \end{cases}, \qquad (11)$$

where p is the pitch, N_t is the number of transducer elements, f_s denotes the sampling frequency, c is the speed of sound and N_r is the number of samples in the axial direction. The discretized preprocessed spectrum is obtained by discretizing the different continuous operations defined in Section III for all the methods. For Lu and Garcia methods, the preprocessing step amounts to compute $\mathbf{y} = \mathsf{F_R}\mathbf{r}$, where $\mathsf{F_R}$ denotes the discrete 2D FT on the k-space defined in (11). For UFSB, the preprocessing step to obtain $\mathbf{y}$ from $\mathbf{r}$ is described in Section III-C for each steering angle θ_r.

Let us also define a discrete uniform grid for the desired RF image space, not necessarily the same grid as the backscattered echo signals:

$$\begin{cases} \boldsymbol{x} &= \left\{\frac{mL}{N_X}, \ \forall m \in \left\{-\frac{N_X}{2}, ..., \frac{N_X}{2} - 1\right\}\right\} \\ \boldsymbol{z} &= \left\{\frac{lZ_{max}}{N_Z}, \ \forall l \in \{0, ..., N_Z - 1\}\right\} \end{cases} \qquad (12)$$

with L the width of the probe, N_X the number of image samples in the lateral direction, N_Z the number of image samples in the axial direction and Z_{max} the maximum depth. The following grid of the corresponding image k-space can be deduced from (12):

$$\begin{cases} \boldsymbol{k'_x} &= \left\{\frac{2\pi m}{L}, \ \forall m \in \left\{\frac{-N_X}{2}, ..., \frac{N_X}{2} - 1\right\}\right\} \\ \boldsymbol{k'_z} &= \left\{\frac{2\pi l}{Z_{max}}, \ \forall l \in \{0, ..., N_Z - 1\}\right\} \end{cases}. \qquad (13)$$

In order to take advantage of the FFT we use the non-uniform fast Fourier transform (NUFFT) to implement the 2D NUFT. The NUFFT operator can be modelled as $\Phi = \mathsf{GF_S}$,

where $\mathsf{F_S}$ denotes the 2D FFT operator that computes the FT of s in the discrete k-space $(\boldsymbol{k'_x}, \boldsymbol{k'_z})$ and $\mathsf{G} \in \mathbb{R}^{N_r N_t \times N_X N_Z}$ is a sparse matrix implementing a convolutional interpolation operator that models the map from the discrete frequency grid onto the continuous values $(\boldsymbol{k_x}, \boldsymbol{k})$ according to the different remappings described in Section III. We thus have the following linear model:

$$\boldsymbol{y} = \mathsf{GF_S}\boldsymbol{s} + \boldsymbol{n} = \Phi\boldsymbol{s} + \boldsymbol{n}, \qquad (14)$$

where $\boldsymbol{n}$ accounts for the measurement noise and model inaccuracies induced by the interpolation.

3) The sparsifying model: The second pillar of the proposed method resides in the existence of a sparsifying model Ψ, *i.e.* a model in which the US images are compressible meaning that their representation in this model contains many zeroes. In the literature, various models have already been proposed mainly relying on wavelet-based models [32], [34], [36], [43]. However, the choice of the best model is a hard task since it is highly dependent on the content of the image, unknown a priori. In this paper, we propose to investigate different sparsifying models described below:

- **Dirac basis**: In this very simple model, the operator Ψ is the identity. This model is suited to images made of few sparse sources.
- **Orthogonal wavelet transform**: In this model, the operator Ψ is the wavelet transform. This model is suited for images with textural information.
- **Undecimated wavelet transform**: In this model, the operator Ψ is a slight variation of the wavelet transform where each decomposition has the same size as the original image [44].
- **Sparsity averaging model (SA)**: The operator for the SA model is composed of the concatenation of Daubechies wavelet transforms with different wavelet mother functions ranging from Daubechies 1 (Db1) to Daubechies 8 (Db8) as it has already been proposed in previous studies [42], [45]. Thus,

$$\Psi = \frac{1}{\sqrt{q}}[\Psi_1, ..., \Psi_q] \qquad (15)$$

where $q = 8$ and Ψ_i denotes i-th Daubechies wavelet. Db1 is the Haar basis promoting piece-wise smooth signals while Db2 to Db8 provide smoother sparse decompositions.

4) The ℓ_1-minimization algorithm: The proposed imaging method is based on solving the convex problem:

$$\min_{\bar{\boldsymbol{s}} \in \mathbb{C}^N} \|\Psi^\dagger \bar{\boldsymbol{s}}\|_1 \text{ subject to } \|\boldsymbol{y} - \Phi\bar{\boldsymbol{s}}\|_2 \leq \epsilon, \qquad (16)$$

where $\Psi^\dagger$ denotes the adjoint operator of Ψ and Φ is the NUFT operator. The alternating direction method of multipliers (ADMM) [46] is chosen to solve (16). The detailed implementation of ADMM can be found in Appendix.

One important aspect in solving problem (16) is the ability to identify the value of ϵ that maximizes the quality of the reconstruction. In the presence of Gaussian noise, a closed-form formulation of the best threshold exists based on the bound of a $\mathcal{X}^2$ distribution [47]. When the noise is not Gaussian,

other methods such as least angle regression (LARS) [48], Pareto-curve-based ℓ_1- algorithms [49] and Stein unbiased risk estimator (SURE) [50] may be used.

In the case of US imaging, the noise is unknown which makes the use of the above methods very hard. Thus, the choice of the best values is, in most of the studies, based either on cross-validation techniques or manually tuned.

The impact of the choice of ϵ on the quality of the reconstruction will be studied in Section VI-B.

C. Compounding scheme for sparse-based beamforming

A common way to increase the contrast of PW imaging methods is by performing compounding of PWs with various steering angles [10], [16]. Since speckle in the images coming from PWs with different angles is decorrelated, averaging the images obtained with several PWs leads to an increase of the contrast. In the special case of Fourier-based methods, using compounding also allows to populate more densely the image spectrum and thus to reduce the interpolation error. It has also been described that the resolution slightly increases with compounding [16].

Formally, let us introduce a set of T emitting angles $(\theta_{t_i})_{i \in \{1,..,T\}}$ and the corresponding backscattered echo signals $(\boldsymbol{r_i})_{i \in \{1,..,T\}}$. The proposed method consists in considering the new measurement vector which concatenates the different preprocessed spectra for all the emitting angles $\boldsymbol{y_C} = [\boldsymbol{y_1}, \boldsymbol{y_2}, ..., \boldsymbol{y_T}]^T$ and the new measurement operator which corresponds to the concatenation of the measurement operators for each emitting angle $\Phi_\mathsf{C} = [\Phi_1, \Phi_2, ..., \Phi_T]^T$. Then, the following problem, close to problem (16), is solved:

$$\min_{\bar{\boldsymbol{s}} \in \mathbb{C}^N} \|\Psi^\dagger \bar{\boldsymbol{s}}\|_1 \text{ subject to } \|\boldsymbol{y_C} - \Phi_\mathsf{C}\bar{\boldsymbol{s}}\|_2 \leq \epsilon, \qquad (17)$$

This problem is solved using the same algorithm as problem (16).

V. EXPERIMENTS

A. Settings

1) Experimental settings: All the measurements have been made with a standard linear-probe whose settings are given in Table I. Several PWs are emitted in order to perform PW

Parameter	Value
Number of elements (N_t)	128
Center frequency (f_0)	5 MHz
Wavelength (λ)	0.31 mm
Sampling frequency (f_s)	31.2 MHz
Pitch (p)	0.193 mm
Kerf	0.05 mm

TABLE I: Probe characteristics.

compounding. For a desired number of PWs, the compounding scheme used is based on steering the PW by $+0.5°$ or $-0.5°$ starting from normal incidence. For instance, if we consider a 3 PWs configuration, the angles are $(-0.5°, 0°, 0.5°)$. Constant speed of sound is assumed (1540 $m.s^{-1}$). No apodization is used neither in transmit nor in receive. The desired RF image is reconstructed from the backscattered echo signals

using classical Fourier-based and delay-and-sum approaches as well as using the proposed approach. The envelope image is extracted from the RF image through the Hilbert transform, gamma-compressed using $\gamma = 0.3$ and finally converted to 8-bit gray scale to get the B-mode image.

2) Image reconstruction: For the classical approaches, a zero-padding of a factor 2 in the axial direction and of a factor 1.5 in the lateral direction is performed for the Fourier-based approaches in order to increase the image quality [37]. The frequency remapping is performed using a linear interpolation.

For the proposed approach, no-zero padding is performed. Four different sparsifying models are tested namely, the Dirac model, the orthogonal wavelet transform (Daubechies 4 wavelets), the undecimated wavelet transform (Daubechies 4 wavelet) and the SA model (Daubechies 1 to Daubechies 8 wavelets). Different values of the sparsifying promoting parameter ϵ are tested ranging between 0 and $||\boldsymbol{y}||_2$.

B. Numerical simulation

We firstly simulate the system described above using CRE-ANUIS [51], [52]. We use a cyst composed of a 8-mm diameter anechoic occlusion centered at 4 cm depth embedded in a medium with high density of scatterers (30 scatterers per resolution cell) whose amplitudes are distributed according to a standard normal distribution.

C. In vitro and in vivo experiments

The measurements are performed using a Verasonics ultrasound scanner (Redmond, WA, USA) with a L12-5 50mm probe with the same settings as the simulated probe (given in Table I). Two types of experiments are made using this setup. Firstly, a CIRS ultrasound phantom (Model 54GS, Computerized Imaging Reference Systems Inc., Norfolk, USA) is imaged. Figure 2 displays the schematic diagram of the corresponding phantom along with the imaging plane used in the experiment. Secondly, *in vivo* carotids are imaged.
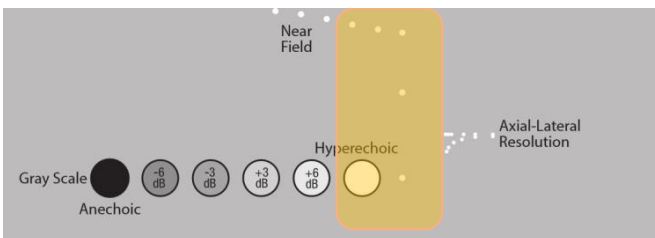

Fig. 2: Schematic diagram of the CIRS phantom with the considered imaging plane (orange region).

VI. RESULTS

A. Choice of the sparsifying model

In order to study the effect of the sparsifying model on the quality of reconstruction, the RF image of the simulated phantom is reconstructed with the four sparsifying models described in Section IV-B3, with $\epsilon = 0.3||\boldsymbol{y}||_2$ and for 1

PW insonification. The contrast [53] is calculated on the normalized envelope image using the following formula:

$$CR = 20 \log_{10} \frac{|\mu_t - \mu_b|}{\sqrt{\frac{\sigma_t^2 + \sigma_b^2}{2}}} \tag{18}$$

where μ_t and μ_b (σ_t^2, σ_b^2) are the means (variances) of respectively the target and the background.

The contrast values, corresponding to the proposed reconstruction coupled with the UFSB method, for the different sparsifying models, are reported on Table II. They indicate that the contrast is higher with the wavelet-based models than with the Dirac basis. This result has been expected since US images are sparser in the wavelet-based models than in the Dirac basis. Among the wavelet-based models, SA performs slightly better than the other models since it preserves a wider range of variations of the signals [42], [45].

	Dirac	Orth. Wavelet	Und. Wavelet	SA
CR (dB)	7.18	8.05	8.30	8.72

TABLE II: Contrast values in dB obtained with 1 PW insonification on the simulated anechoic phantom. The reconstruction is performed with the proposed approach (UFSB method) and four different sparsifying models.

It is known that the envelope image of diffusive speckle follows a Rayleigh distribution [54], [55]. In order to evaluate the reconstruction of the textured area, where diffusive speckle should be present, the goodness-of-fit against the Rayleigh distribution is tested. The envelope image is divided into non-overlapping blocks of 10×10 pixels. In each block, a one-sample Kolmogorov-Smirnov (KS) test is performed. This test is a widely used statistical hypothesis test that can be used to verify the equality between a sample and a reference continuous probability density function (pdf). In our study, the null hypothesis states that the envelope image follows a Rayleigh distribution with significance level $\alpha = 0.05$. For a random variable r, the pdf of the Rayleigh distribution is given by $p(r) = \frac{r}{\sigma^2} e^{-\left(\frac{r^2}{2\sigma^2}\right)}$ and thus requires the estimation of the variance σ^2. The parameter is estimated using the maximum likelihood method which solution has the following closed-form: $\sigma_{ML} = \frac{E(r^2)}{2}$ with $E(r)$ the mean of the random variable r [56]. The blocks that pass the KS test are included in the speckle region.

In order to quantify the reconstruction of the textural information, we reconstruct the simulated cyst with the proposed approach (and UFSB) for 1 PW insonification and for the four sparsifying models. We segment the reconstructed images into two area, namely the *anechoic area* (pixels inside the occlusion) and the *fully developed speckle area*, by considering that the *anechoic area* is composed of the pixels inside the circle centered in $(0, 40)$ (mm) with a radius of 4 mm. Then, we calculate the number of non-overlapping blocks of 10×10 pixels of the *fully developed speckle area* which pass the KS test for the four different sparsifying models. We divide the obtained values by the number of non-overlapping blocks of 10×10 pixels present in the *fully developed speckle area*. The
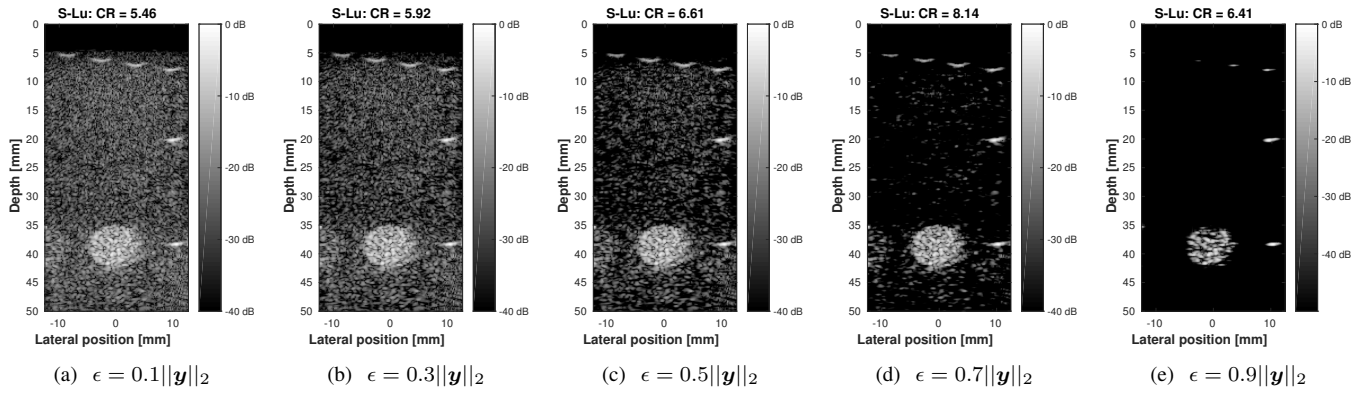
Fig. 3: B-mode images of the hyperechoic CIRS phantom using the proposed method coupled with Lu method for different values of ϵ and for 1 PW insonification.

results, expressed in % and given in Table III, show that wavelet-based models allow to recover more accurately the speckle texture than the Dirac basis. Among the three wavelet-based models, the SA model preserves best the speckle texture.

	Dirac	Orth. Wavelet	Und. Wavelet	SA
% of diffusive area	38 %	43 %	48 %	50 %

TABLE III: Percentage of diffusive speckle accurately reconstructed by the proposed approach (UFSB method) and four different sparsifying models.

In the next sections, the SA model has been chosen as the sparsifying model since it enables a slightly better reconstruction than other wavelet-based models.

B. Study of the optimization parameter

In this section, the impact of the optimization parameter on the image quality is investigated. The parameter of interest is ϵ of equation (1) which corresponds to a higher bound of the distance (given by the ℓ_2-norm) between the data and the desired solution. In this sense, the value of ϵ quantifies the relative weight between the data fidelity constraint and the sparsity prior applied on the desired image.

In order to analyse the effect of ϵ on the image quality, B-mode images of the hyperechoic occlusion of the CIRS phantom, present in the image plane 1, are displayed for different values of ϵ ranging from $0.1||\boldsymbol{y}||_2$ to $0.9||\boldsymbol{y}||_2$. The images, reported on Figure 3 show that when the value of ϵ increases, the speckle density tends to decrease until the speckle totally disappears (Fig. 3d). In this case, while the CR is maximized, it is clear that the image is over-regularized.

To illustrate what we mentioned before, Figure 4 displays the evolution of both the contrast and the percentage of recovered diffuse speckle area, calculated with the same process as in Section VI-A, for an increasing value of the sparsity promoting parameter. It can be observed that, while the contrast keeps increasing, the speckle density tends to decrease when sparsity in the SA model is promoted in the reconstruction.
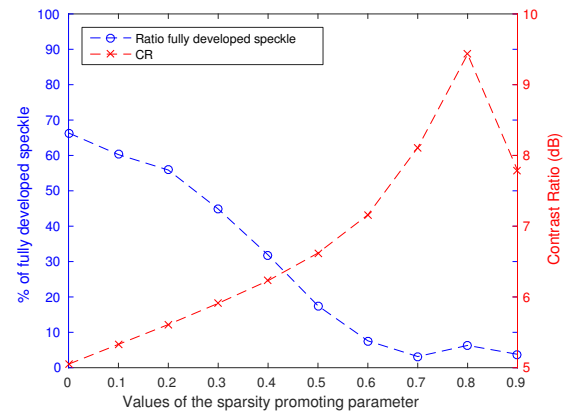

Fig. 4: Evolution of the contrast ratio (red) and the percentage of recovered speckle density for increasing values of the sparsity promoting parameter. The metrics have been calculated on the images obtained with 1 PW insonification and reconstructed using the sparse-based approach with Lu method.

The study shows that part of the diffusive speckle is not sparse enough in the proposed model and then considered as noise. It is clear that the choice of the right parameter highly depends on both the image content and the user needs. If speckle is considered as noise, then it can be removed by forcing sparsity in a wavelet-based model. If both speckle and texture have to be preserved, a low value of ϵ (between $0.1||\boldsymbol{y}||_2$ and $0.3||\boldsymbol{y}||_2$ for Figure 3) seems to be a good trade-off between an increase of the contrast and a reasonable speckle density.

C. Comparison against classical approaches

1) Contrast: Figure 5 displays the CR values for the proposed method and for the state of the art methods for each compounding experiment, with $\epsilon = 0.3||\boldsymbol{y}||_2$. It shows that the proposed method leads to an increase of the contrast of more than 2.5 dB for 1 PW. This gap decreases with compounding since the CR increases far faster for the classical methods than for the proposed method. This can be explained by the fact that compounding decreases the noise level by decorrelating
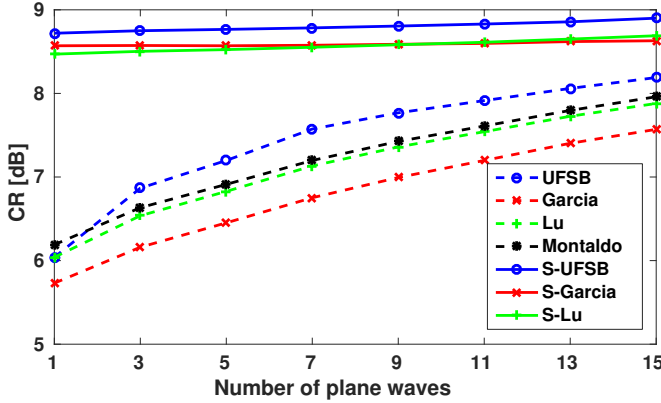
Fig. 5: Contrast ratio as a function of the number of PWs for the different reconstruction methods. The dashed lines represent the classical methods and the solid lines represent the sparse-based method.

the random speckle [10]. The proposed method also removes the measurement noise by enforcing sparsity in the SA model. Thus, the two methods inducing the same consequence, the impact of the compounding in terms of noise removal is less important. However, it is interesting to note that the proposed method, with 1 PW, leads to higher contrasts than classical methods with 15PWs, thus achieving a noticeable reduction of the measurements needed to reach a given image quality.

Figure 6 confirms what we deduced from the contrast measurement. The proposed method removes the noise inside the inclusion which appears with the classical methods. It can also be observed that the speckle density slightly decreases in the far field for the proposed method. This aspect will be discussed in Section VI-C3.

Since the contrast is measured in the anechoic area, it is directly linked to the amount of noise in the image and since the simulation is noiseless, the only source of noise in the experiment is induced by the approximation of the measurement model. The proposed approach leads to an increase of the contrast thus to a decrease of the noise created by the measurement model, which means that the proposed measurement process is more accurate than the classical filtered back projection.

2) Resolution: The lateral resolution is calculated on the B-mode image as the width at -6 dB of the point spread function (PSF) of the two points at 2cm and 4cm of the CIRS phantom which corresponds to the full width at half maximum [53]. Figure 7 displays the evolution of the lateral resolution with the number of PWs for the different reconstruction methods.

From Figure 7, it can be observed that the proposed method leads to a slight increase of the image resolution. This may be justified by the fact that the proposed method significantly decreases the magnitude of the side lobes of the PSF.

From Figure 7a, it can be noticed that the proposed approach gives results similar to the classical approach except for Lu method in which the resolution is better with the proposed approach.

From Figure 7b, it can be noticed that the proposed method leads to a slight increase of the resolution for UFSB. For

Garcia and Lu methods, the resolution is rather similar. For Garcia method, it can also be observed that the resolution decreases when the number of PWs increases. While being counter-intuitive, this result is in accordance with what Garcia *et al.* observed [16].

On Figure 8, the effect of the proposed method on the PSF is investigated. It can be observed that the proposed method drastically decreases the magnitude of the side lobes. This observation is in accordance with the results observed in Section VI-C.

3) Speckle density: On Figure 6, it can be noticed that the speckle density seems to be lower for the proposed approach than for the classical methods. In order to quantify the impact of the proposed approach on the texture, the same procedure as for the texture experiment in Section VI-A is followed for both the proposed approach and the classical methods. The percentages of the total diffusive speckle area recovered with the classical methods are 66% for Lu method, 59% for UFSB and 62% for Garcia method. These results are around 10% higher than the ones obtained with the proposed approach (Table III). The difference is justified by the fact that speckle has a very complex behaviour, which is different at each depth. This complex structure is very hard to preserve and fully developed speckle is not sufficiently sparse even in complex wavelet-based models. This aspect will be discussed in Section VII-B.

D. In vivo experiments

The proposed approach is finally evaluated on *in vivo* carotid images. Since the ground truth is not known, the use of the metrics defined in Section VI-A is not anymore possible.

In the experiments, the images are reconstructed with only 1 PW insonification. The sparsity promoting parameters have been manually tuned based on visual evaluation of the reconstructed image. From Figure 9, it can be seen that part of the noise in the carotid artery and between 5 mm and 15 mm have been removed. Moreover, the proposed method reduces the side lobes as it can be seen particularly close to the upper carotid wall. However, as expected from the study of Section VII-B, the speckle density in the far field (farther than 20mm) is lower with the proposed approach than with classical methods.

As a reference, Figure 10 displays the B-mode image of the DAS reconstruction obtained with 15 PWs. It can be seen that the proposed reconstruction leads to a visual quality closer to the one of Figure 10 than the classical methods.

VII. DISCUSSION

A. The use of sparse regularization to solve the problem

The use of sparse regularization to solve the ill-posed problem mainly comes from CS framework and the assumption that US images are compressible in well chosen models. One can question the use of sparsity prior as an appropriate regularizer for the problem. Another alternative may be to use ℓ_2-norm and perform an inversion similar to Wiener filtering [57]. The main advantage of this approach resides in its simple implementation since a closed form formula exists for the
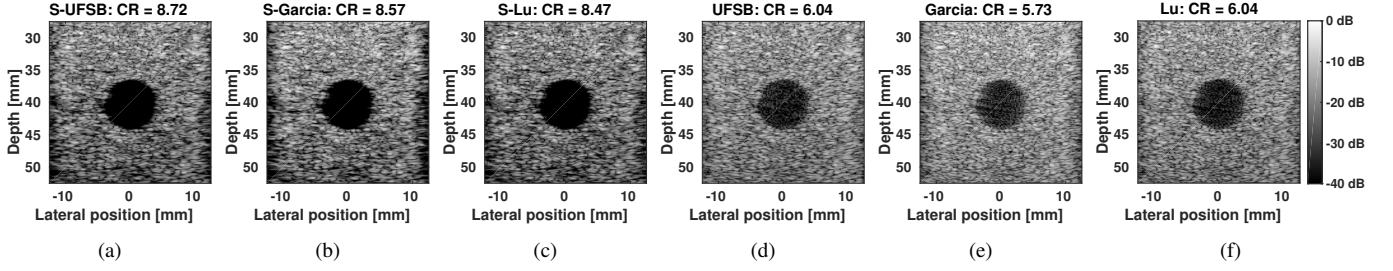
Fig. 6: B-mode images of the simulated occlusion using the proposed method with (a) UFSB, (b) Garcia and (c) Lu and using the classical method with (d) UFSB, (e) Garcia and (f) Lu for 1 PW insonification.
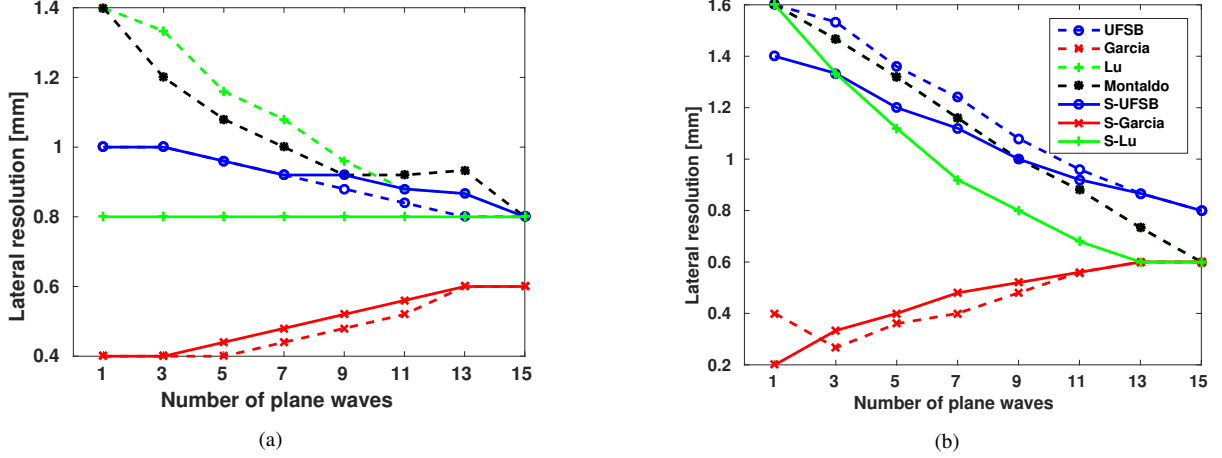

Fig. 7: Lateral resolution measured on the points of the CIRS phantom located at a depth of (a) 2 cm and (b) 4 cm for different compounding experiments.
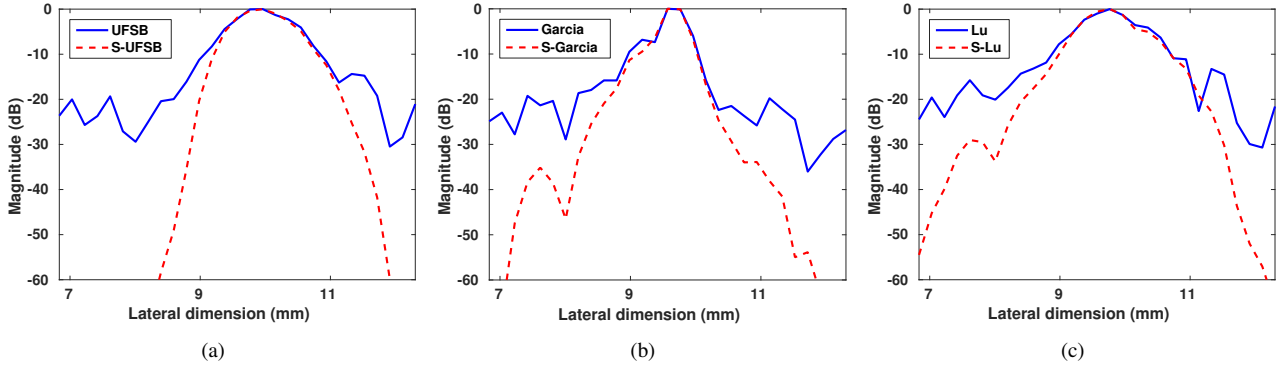

Fig. 8: Lateral point spread function measured on the point of the CIRS phantom located at a depth of 2 cm, for 1 PW insonification, and reconstructed with (a) UFSB, (b) Garcia and (c) Lu. The red dashed line represents the proposed method and the blue line corresponds to the classical method.

ℓ_2-regularization problem. Nonetheless, the perfect recovery condition that holds for ℓ_1-regularization does not remain valid for ℓ_2-regularization. Additionally, in practice, the quality of the reconstruction (in terms of contrast and resolution) is lower with ℓ_2-regularization than with ℓ_1-regularization methods since Wiener filtering tends to smooth the information in the ultrasound images [58], [59] .

The ℓ_1-norm is used in the optimization problem as sparsity promoting norm. The choice of such norm against ℓ_p-norm with $p < 1$ is justified firstly by the convexity of the optimization problem, leading to a unique solution and secondly by the

availability of an extensive number of methods to solve such problem. One can suggest the use of reweighted ℓ_1-algorithms [45], [60] as an alternative to the proposed approach. While being a better approximate of the ℓ_0-norm, it requires many iterations of the optimization algorithm. Our main motivation of using ℓ_1- algorithms instead of reweighting ℓ_1-algorithms is convergence time.

Several studies have used ℓ_p-norm with $p \in]1, 2]$ instead of ℓ_1-norm due to the statistical behaviour of scatterers map, closer to Generalized Gaussian model than to Laplacian model [32], [57]. In the proposed approach, the choice of the ℓ_1-norm
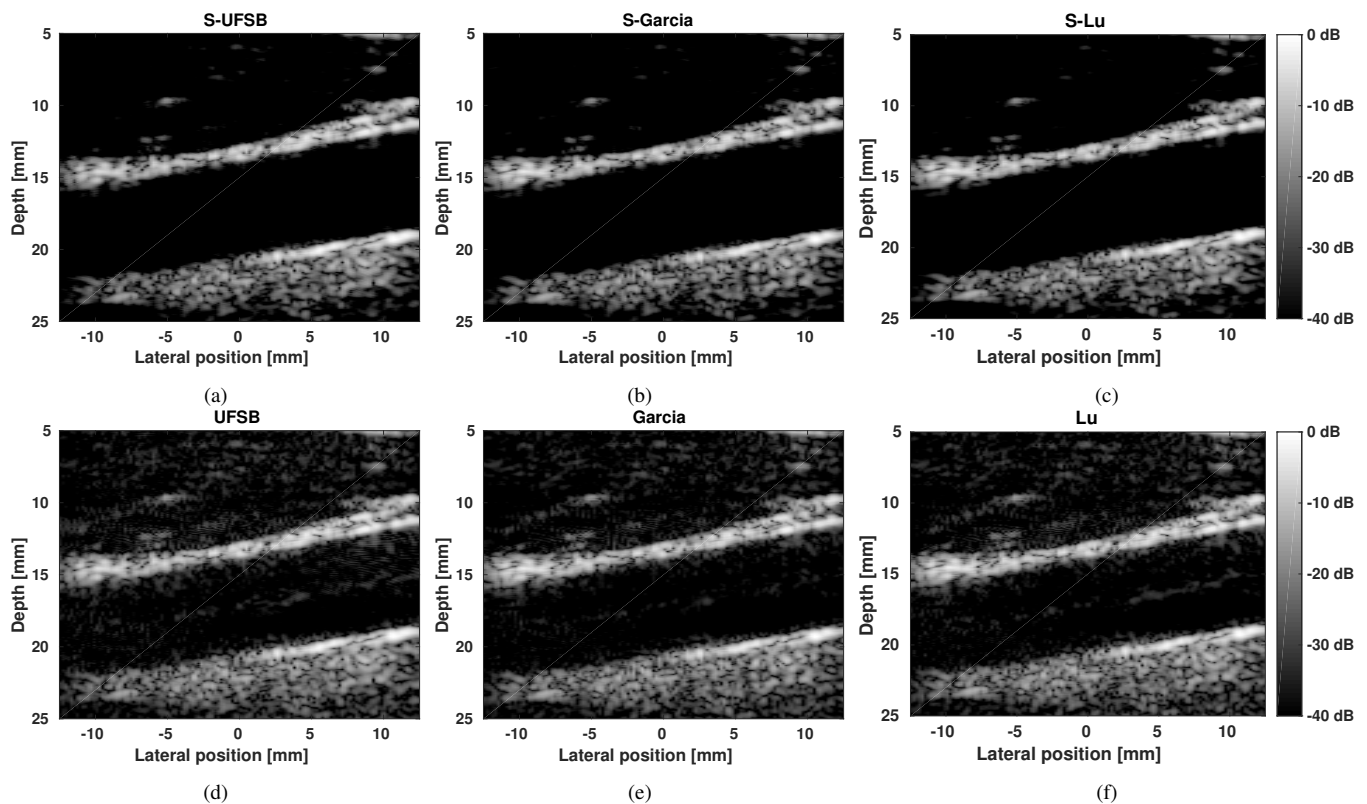
Fig. 9: B-mode images of the carotid phantom using the proposed method with (a) UFSB, (b) Garcia and (c) Lu and using the classical method with (d) UFSB, (e) Garcia and (f) Lu for 1 PW insonification.
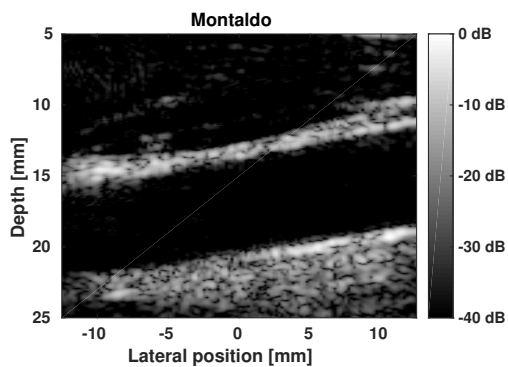

Fig. 10: B-mode image of the DAS reconstruction with 15 PWs.

in a given model is motivated by geometrical considerations more than statistical prior. In the above mentioned approaches, the US image is deconvolved and statistical priors are assumed on the deconvolved image, usually called tissue reflectivity function (TRF) or scatterers map. In the proposed approach, the unknown image is the RF image which does not necessarily exhibit the same statistical behaviour. This difference is described by Chen *et al.* [32] who present a compressed deconvolution framework in which a sparsity prior in the wavelet domain is used for the RF image and Generalized Gaussian Distribution prior is used for the TRF.

With the current implementation of the inverse problem, the resolution is not improved. However, the proposed approach is compatible with the state-of-the-art deconvolution frameworks such as the compressive deconvolution framework [32]. By combining the two approaches, it would be possible to improve the resolution.

B. Speckle density

While it has been demonstrated that a wavelet-based model enables better capturing textural information of images than a Dirac basis, part of the speckle remains being considered as measurement noise, showing that fully developed speckle is not entirely sparse in wavelet-based models. This is a limitation of the proposed approach and we can think about two ways to overcome these drawback. The first one is to perform region-based optimization. The idea would be to segment US images in different regions either in a very simple way (by dividing the image into blocks of fixed size) or with more elaborated segmentation methods based on structural information inside regions [61]. Then, the optimization problems are solved on each region independently allowing to adapt the reconstruction to the content of each region. The main drawback of such optimization is the computational complexity as well as the need for a stitching method to reconstruct the full image from the different regions. The other alternative resides in performing dictionary learning [33]. With such approach, the analysis model is learnt on a training set and a sparser representation of the speckle may be found. This would very probably leads to better results. Nonetheless, this approach requires an extensive number of ultrasound images

in the training set in order to cover all the possible cases of diffusive speckle and the related analysis model is very complex.

C. Computational complexity

Solving ℓ_1-regularized problems to reconstruct the desired image usually involves non-linear iterative algorithms. Thus, computational complexity is a problem to take into account when using these methods. Indeed, considering the scheme of the ADMM algorithm in appendix, it can be seen that the algorithm is composed of a gradient descent and a soft-thresholding in the analysis domain. This implies two matrix products with Φ and $\Phi^\dagger$ for the gradient descent and two matrix products with $\Psi^\dagger$ and Ψ, respectively, for the soft-thresholding operation. Since the matrix Ψ is made of a concatenation of wavelet bases, its size is several times the size of the image, depending on the number of wavelet bases considered. Doing the matrix product is then costly. A way to address such problem is by considering parallel implementation of wavelets on GPU and to exploit fast algorithms to implement the wavelet decomposition with $O(N \log N)$ complexity.

Regarding the matrix Φ, the NUFFT algorithm proposed by Fessler and Sutton [62] consists in a zero padded 2D FFT followed by an interpolation step to compute the values outside the regular grid. The operator can be modelled as $\Phi = \mathsf{GFZ}$, where Z denotes the zero padding operator, F denotes the 2D FFT operator (in the upsampled size) and G is a sparse matrix implementing the convolutional interpolation operator. Considering that the desired image is composed of N pixels, that the number of resampled frequency locations is $K = 2N$ (typical value), that M is the number of non-uniform frequencies and that the interpolation neighbourhood is J, it has been demonstrated that the computational complexity of the NUFFT is $O(K \log N + JM)$ [37]. Since it depends both on the number of non-uniform frequency samples and on the number of points in the final image, it is far more complex than the FFT and becomes extremely slow when used in a compounding scheme where the total number of frequencies, M, is large.

One alternative to speed up the reconstruction algorithm is to grid the measured data onto a regular grid, i.e. $\boldsymbol{y}' = \mathsf{G}^T \boldsymbol{y}$, and approximate the NUFFT by an FFT followed by mask on the sensed discrete frequencies, i.e. $\Phi = \mathsf{MF}$, where F denotes the 2D FFT of size N and M is a $Q \times N$ diagonal binary matrix that selects the sensed discrete frequencies. Indeed, the later model approximates the holographic matrix $\mathsf{G}^T \mathsf{G}$, that grids the continuous frequency samples back to the uniform grid, by the diagonal binary matrix M. This simplified model allows us to drastically decrease the complexity of the operator Φ while preserving the reconstruction quality almost intact.

D. Fourier-based beamforming methods

To the best of our knowledge, Fourier-based beamforming methods have been investigated by Chernyakova *et al.* [35]. In their work, they introduced the beamforming in the frequency domain as an alternative to the classical DAS beamforming.

The objective is to exploit the band-limited properties of US signals in order to drastically reduce the data rate compared to classical approach.

In a second step, they suggest to use CS in order to further decrease the data rate. In this case, the Fourier series coefficients of the beamformed signal are expressed as a sum of phase-shifted pulse shapes, with a given amplitude, through a finite rate of innovation model. CS framework is used to retrieve the pulse amplitudes from the Fourier series coefficients.

Thus, the work proposed by Chernyakova *et al.* is, by essence, different from the proposed approach. First, the objective is different since the proposed work focuses on improving the results of the plane wave reconstruction while the work of Chernyakova *et al.* emphasizes the data rate reduction. Moreover, while the work of Chernyakova *et al.* exploits CS in order to retrieve pulses amplitudes later used to reconstruct the RF image, the proposed work uses CS as a way to recover the RF image coefficients directly.

VIII. CONCLUSION

In this paper, a novel framework for Fourier-based reconstruction of signals obtained with several PW insonifications has been proposed. The framework relies on the ability to pose the Fourier reconstruction problem as an ill-posed inverse problem and and on the sparsity of the US images in an analysis domain. The reconstruction is achieved by solving an ℓ_1-minimization problem. Different sparsifying transforms have been studied and the SA model exhibits better reconstruction results than other wavelet-based models. Simulations and experiments enlighten a better image quality (contrast) for the proposed approach than for the state-of-the-art methods with a slight decrease of the speckle density. This decrease comes from the fact that fully developed speckle is not entirely sparse in the proposed analysis models. However, the proposed framework opens the door to a variety of promising applications such as compressed beamforming and deconvolution.

APPENDIX: ADMM ALGORITHM

The pseudo-code of the ADMM algorithm used in the proposed method is given below. The general problem we solve is the following one:

$$\min_{\boldsymbol{x} \in \mathbb{C}^N, \boldsymbol{z} \in \mathbb{C}^M} f(\boldsymbol{x}) + h(\boldsymbol{z}) \text{ subject to } \Phi \boldsymbol{x} + \boldsymbol{z} = \boldsymbol{y}, \quad (19)$$

given the assumption that $f : \mathbb{C}^N \to \mathbb{R}$ and $h : \mathbb{C}^M \to \mathbb{R}$ are lower semicontinuous convex functions.

The key mathematical tool used in ADMM is the proximity operator of a convex function defined as:

$$\text{prox}_f(\boldsymbol{x}) = \arg \min_{\boldsymbol{y} \in \mathbb{C}^M} f(\boldsymbol{y}) + \frac{1}{2}||\boldsymbol{y} - \boldsymbol{x}||_2^2. \quad (20)$$

In the proposed ℓ_1-minimization problem $f(\boldsymbol{x}) = ||\Psi^\dagger \boldsymbol{x}||_1$ and $h(\boldsymbol{z}) = i_B(\boldsymbol{z})$, where i_B is the indicator function of the convex set B defined as $B = \{z \in \mathbb{C}^M | ||\boldsymbol{z}||_2 \le \epsilon\}$.

The general structure of the algorithm is detailed in Algorithm 1. The parameters $\mu > 0$ and $\beta > 0$ are step sizes chosen such that $\mu L + \beta < 2$, where L is the spectral norm of the matrix Φ, and $\gamma > 0$ is a thresholding constant that controls the convergence speed.

Algorithm 1 ADMM algorithm

Require: $t = 0$, choose $\boldsymbol{x^0}, \boldsymbol{z^0}, \boldsymbol{\lambda^0}, \gamma, \mu$ and β.
  repeat
    $\boldsymbol{z}^{(t+1)} = \text{prox}_{\gamma h}(\boldsymbol{y} - \Phi\boldsymbol{x}^{(t)} - \boldsymbol{\lambda}^{(t)})$
    $\boldsymbol{s}^{(t+1)} = \boldsymbol{x}^{(t)} - \mu\Phi^H\left(\boldsymbol{\lambda}^{(t)} + \Phi\boldsymbol{x}^{(t)} - \boldsymbol{y} + \boldsymbol{z}^{(t+1)}\right)$
    $\boldsymbol{x}^{(t+1)} = \text{prox}_{\mu\gamma f}\left(\boldsymbol{s}^{(t+1)}\right)$
    $\boldsymbol{\lambda}^{(t+1)} = \boldsymbol{\lambda}^{(t)} + \beta\left(\Phi\boldsymbol{x}^{(t+1)} - \boldsymbol{y} + \boldsymbol{z}^{(t+1)}\right)$
  until A stopping criterion is met

REFERENCES

[1] J. Ylitalo and H. Ermert, "Ultrasound synthetic aperture imaging: monostatic approach," *IEEE Trans. Ultrason. Ferroelectr. Freq. Control*, vol. 41, no. 3, pp. 333–339, may 1994.

[2] J. A. Jensen, S. I. Nikolov, K. L. Gammelmark, and M. H. Pedersen, "Synthetic aperture ultrasound imaging," *Ultrasonics*, vol. 44, pp. e5–e15, dec 2006.

[3] J. Bercoff, M. Tanter, and M. Fink, "Supersonic shear imaging: a new technique for soft tissue elasticity mapping." *IEEE Trans. Ultrason. Ferroelectr. Freq. Control*, vol. 51, no. 4, pp. 396–409, apr 2004.

[4] S. Salles, A. J. Y. Chee, D. Garcia, A. C. H. Yu, D. Vray, and H. Liebgott, "2-D arterial wall motion imaging using ultrafast ultrasound and transverse oscillations," *IEEE Trans. Ultrason. Ferroelectr. Freq. Control*, vol. 62, no. 6, pp. 1047–1058, jun 2015.

[5] J. Udesen, F. Gran, K. Hansen, J. Jensen, C. Thomsen, and M. Nielsen, "High frame-rate blood vector velocity imaging using plane waves: Simulations and preliminary experiments," *IEEE Trans. Ultrason. Ferroelectr. Freq. Control*, vol. 55, no. 8, pp. 1729–1743, aug 2008.

[6] J. Bercoff, G. Montaldo, T. Loupas, D. Savery, F. Meziere, M. Fink, and M. Tanter, "Ultrafast compound doppler imaging: providing full blood flow characterization," *IEEE Trans. Ultrason. Ferroelectr. Freq. Control*, vol. 58, no. 1, pp. 134–147, jan 2011.

[7] M. Lenge, A. Ramalli, P. Tortoli, C. Cachard, and H. Liebgott, "Plane-wave transverse oscillation for high-frame-rate 2-D vector flow imaging," *IEEE Trans. Ultrason. Ferroelectr. Freq. Control*, vol. 62, no. 12, pp. 2126–2137, dec 2015.

[8] O. Couture, S. Bannouf, G. Montaldo, J.-F. Aubry, M. Fink, and M. Tanter, "Ultrafast Imaging of Ultrasound Contrast Agents," *Ultrasound Med. Biol.*, vol. 35, no. 11, pp. 1908–1916, nov 2009.

[9] M. Tanter and M. Fink, "Ultrafast imaging in biomedical ultrasound," *IEEE Trans. Ultrason. Ferroelectr. Freq. Control*, vol. 61, no. 1, pp. 102–119, 2014.

[10] G. Montaldo, M. Tanter, J. Bercoff, N. Benech, and M. Fink, "Coherent plane-wave compounding for very high frame rate ultrasonography and transient elastography," *IEEE Trans. Ultrason. Ferroelectr. Freq. Control*, vol. 56, no. 3, pp. 489–506, mar 2009.

[11] J.-Y. Lu and J. F. Greenleaf, "Pulse-echo imaging using a nondiffracting beam transducer." *Ultrasound Med. Biol.*, vol. 17, no. 3, pp. 265–81, 1991.

[12] J.-Y. Lu and J. Greenleaf, "Ultrasonic nondiffracting transducer for medical imaging," *IEEE Trans. Ultrason. Ferroelectr. Freq. Control*, vol. 37, no. 5, pp. 438–447, sep 1990.

[13] ——, "Experimental verification of nondiffracting X waves," *IEEE Trans. Ultrason. Ferroelectr. Freq. Control*, vol. 39, no. 3, pp. 441–446, may 1992.

[14] J.-Y. Lu, "2D and 3D High Frame Rate Imaging with Limited Diffraction Beams," *IEEE Trans. Ultrason. Ferroelectr. Freq. Control*, vol. 44, no. 4, pp. 839–856, jul 1997.

[15] J. Cheng and J.-Y. Lu, "Extended high-frame rate imaging method with limited-diffraction beams," *IEEE Trans. Ultrason. Ferroelectr. Freq. Control*, vol. 53, no. 5, pp. 880–899, may 2006.

[16] D. Garcia, L. L. Tarnec, S. Muth, E. Montagnon, J. Poree, and G. Cloutier, "Stolt's f-k migration for plane wave ultrasound imaging," *IEEE Trans. Ultrason. Ferroelectr. Freq. Control*, vol. 60, no. 9, pp. 1853–1867, sep 2013.

[17] O. Bernard, M. Zhang, F. Varray, P. Gueth, J.-P. Thiran, H. Liebgott, and D. Friboulet, "Ultrasound Fourier slice imaging: a novel approach for ultrafast imaging technique," in *2014 IEEE Int. Ultrason. Symp.* IEEE, sep 2014, pp. 129–132.

[18] L. Sandrin, S. Catheline, M. Tanter, X. Hennequin, and M. Fink, "Time-resolved pulsed elastography with ultrafast ultrasonic imaging." *Ultrason. Imaging*, vol. 21, no. 4, pp. 259–72, oct 1999.

[19] J. Hsieh, *Computed Tomography, Second Edition*. 1000 20th Street, Bellingham, WA 98227-0010 USA: SPIE, oct 2009.

[20] J. Song, Q. H. Liu, G. A. Johnson, and C. T. Badea, "Sparseness prior based iterative image reconstruction for retrospectively gated cardiac micro-CT," *Med. Phys.*, vol. 34, no. 11, p. 4476, jul 2007.

[21] G.-H. Chen, J. Tang, and S. Leng, "Prior image constrained compressed sensing (PICCS): a method to accurately reconstruct dynamic CT images from highly undersampled projection data sets." *Med. Phys.*, vol. 35, no. 2, pp. 660–3, feb 2008.

[22] E. Y. Sidky and X. Pan, "Image reconstruction in circular cone-beam computed tomography by constrained, total-variation minimization," *Phys. Med. Biol.*, vol. 53, no. 17, pp. 4777–4807, sep 2008.

[23] M. Lustig, D. Donoho, and J. M. Pauly, "Sparse MRI: The application of compressed sensing for rapid MR imaging." *Magn. Reson. Med.*, vol. 58, no. 6, pp. 1182–95, dec 2007.

[24] G. Puy, J. P. Marques, R. Gruetter, J.-P. Thiran, D. Van De Ville, P. Vandergheynst, and Y. Wiaux, "Spread Spectrum Magnetic Resonance Imaging," *IEEE Trans. Med. Imaging*, vol. 31, no. 3, pp. 586–598, mar 2012.

[25] M. Doneva, P. Börnert, H. Eggers, C. Stehning, J. Sénégas, and A. Mertins, "Compressed sensing reconstruction for magnetic resonance parameter mapping," *Magn. Reson. Med.*, vol. 64, no. 4, pp. 1114–1120, jun 2010.

[26] K. T. Block, M. Uecker, and J. Frahm, "Model-Based Iterative Reconstruction for Radial Fast Spin-Echo MRI," *IEEE Trans. Med. Imaging*, vol. 28, no. 11, pp. 1759–1769, nov 2009.

[27] A. Auría, A. Daducci, J.-P. Thiran, and Y. Wiaux, "Structured sparsity for spatially coherent fibre orientation estimation in diffusion MRI," *Neuroimage*, vol. 115, pp. 245–255, jul 2015.

[28] H. Jung, K. Sung, K. S. Nayak, E. Y. Kim, and J. C. Ye, "k-t FOCUSS: A general compressed sensing framework for high resolution dynamic MRI," *Magn. Reson. Med.*, vol. 61, no. 1, pp. 103–116, jan 2009.

[29] R. Otazo, E. J. Candes, and D. K. Sodickson, "Low-rank plus sparse matrix decomposition for accelerated dynamic MRI with separation of background and dynamic components," *Magn. Reson. Med.*, vol. 73, no. 3, pp. 1125–1136, mar 2015.

[30] D. Friboulet, H. Liebgott, and R. Prost, "Compressive sensing for raw RF signals reconstruction in ultrasound," *2010 IEEE Int. Ultrason. Symp.*, pp. 367–370, oct 2010.

[31] C. Quinsac, A. Basarab, and D. Kouamé, "Frequency domain compressive sampling for ultrasound imaging," *Adv. Acoust. Vib.*, vol. 2012, 2012.

[32] Z. Chen, A. Basarab, and D. Kouame, "Compressive Deconvolution in Medical Ultrasound Imaging," *IEEE Trans. Med. Imaging*, pp. 1–1, 2015.

[33] O. Lorintiu, H. Liebgott, A. Martino, O. Bernard, and D. Friboulet, "Compressed sensing reconstruction of 3D ultrasound data using dictionary learning and line-wise subsampling." *IEEE Trans. Med. Imaging*, 2015.

[34] M. F. Schiffner and G. Schmitz, "Pulse-echo ultrasound imaging combining compressed sensing and the fast multipole method," *2014 IEEE Int. Ultrason. Symp.*, pp. 2205–2208, 2014.

[35] T. Chernyakova and Y. Eldar, "Fourier-domain beamforming: The path to compressed ultrasound imaging," *IEEE Trans. Ultrason. Ferroelectr. Freq. Control*, vol. 61, no. 8, pp. 1252–1267, 2014.

[36] G. David, J.-l. Robert, B. Zhang, and A. F. Laine, "Time domain compressive beam forming of ultrasound signals," *J. Acoust. Soc. Am.*, vol. 137, no. 5, pp. 2773–2784, 2015.

[37] P. Kruizinga, F. Mastik, N. de Jong, A. F. W. van der Steen, and G. van Soest, "Plane-wave ultrasound beamforming using a nonuniform fast Fourier transform." *IEEE Trans. Ultrason. Ferroelectr. Freq. Control*, vol. 59, no. 12, pp. 2684–2691, 2012.

[38] D. L. Donoho, "Compressed sensing," *IEEE Trans. Inf. Theory*, vol. 52, no. 4, pp. 1289–1306, 2006.

[39] E. J. Candes, "Compressive sampling," in *Proc. Int. Congr. Math.*, vol. 3. Madrid, Spain, 2006, pp. 1433–1452.

[40] M. Fornasier and H. Rauhut, "Compressive Sensing," in *Handb. Math. Methods Imaging*. New York, NY: Springer New York, 2011, pp. 187–228.

[41] E. J. Candes, Y. C. Eldar, D. Needell, and P. Randall, "Compressed sensing with coherent and redundant dictionaries," *Appl. Comput. Harmon. Anal.*, vol. 31, no. 1, pp. 59–73, 2011.

[42] R. E. Carrillo, A. Besson, M. Zhang, D. Friboulet, Y. Wiaux, J.-P. Thiran, and O. Bernard, "A sparse regularization approach for ultrafast ultrasound imaging," in *IEEE Int. Ultrason. Symp. IUS*, 2015.

[43] M. F. Schiffner and G. Schmitz, "Fast pulse-echo ultrasound imaging employing compressing sensing," *2011 IEEE Int. Ultrason. Symp.*, 2011.

[44] J.-L. Starck, J. Fadili, and F. Murtagh, "The Undecimated Wavelet Decomposition and its Reconstruction," *IEEE Trans. Image Process.*, vol. 16, no. 2, pp. 297–309, feb 2007.

[45] R. E. Carrillo, J. D. McEwen, D. Van De Ville, J.-P. Thiran, and Y. Wiaux, "Sparsity averaging for compressive imaging," *IEEE Signal Process. Lett.*, vol. 20, no. 6, pp. 591–594, 2013.

[46] S. Boyd, "Distributed Optimization and Statistical Learning via the Alternating Direction Method of Multipliers," *Found. Trends. Mach. Learn.*, vol. 3, no. 1, pp. 1–122, 2010.

[47] R. E. Carrillo, J. D. McEwen, and Y. Wiaux, "Purify: A new approach to radio-interferometric imaging," *Mon. Not. R. Astron. Soc.*, vol. 439, pp. 3591–3604, 2014.

[48] R. Tibshirani, I. Johnstone, T. Hastie, and B. Efron, "Least angle regression," *Ann. Stat.*, vol. 32, no. 2, pp. 407–499, apr 2004.

[49] E. van den Berg and M. P. Friedlander, "Probing the Pareto Frontier for Basis Pursuit Solutions," *SIAM J. Sci. Comput.*, vol. 31, no. 2, pp. 890–912, jan 2009.

[50] C.-A. Deledalle, S. Vaiter, J. Fadili, and G. Peyré, "Stein Unbiased GrAdient estimator of the Risk (SUGAR) for Multiple Parameter Selection," *SIAM J. Imaging Sci.*, vol. 7, no. 4, pp. 2448–2487, jan 2014.

[51] F. Varray, A. Ramalli, C. Cachard, P. Tortoli, and O. Basset, "Fundamental and second-harmonic ultrasound field computation of inhomogeneous nonlinear medium with a generalized angular spectrum method," *IEEE Trans. Ultrason. Ferroelectr. Freq. Control*, vol. 58, no. 7, pp. 1366–1376, July 2011.

[52] F. Varray, O. Basset, P. Tortoli, and C. Cachard, "Creanuis: A non-linear radiofrequency ultrasound image simulator," *Ultrasound Med. Biol.*, vol. 39, no. 10, pp. 1915 – 1924, 2013.

[53] M. C. Van Wijk and J. M. Thijssen, "Performance testing of medical ultrasound equipment: Fundamental vs. harmonic mode," *Ultrasonics*, vol. 40, no. 1-8, pp. 585–591, 2002.

[54] R. Wagner, S. Smith, J. Sandrik, and H. Lopez, "Statistics of Speckle in Ultrasound B-Scans," *IEEE Trans. Sonics Ultrason.*, vol. 30, no. 3, pp. 156–163, may 1983.

[55] C. B. Burckhardt, "Speckle in ultrasound B-mode scans," *IEEE Trans. Sonics Ultrason.*, vol. 25, no. 1, pp. 1–6, jan 1978.

[56] B. Raju and M. Srinivasan, "Statistics of envelope of high-frequency ultrasonic backscatter from human skin in vivo," *IEEE Trans. Ultrason. Ferroelectr. Freq. Control*, vol. 49, no. 7, pp. 871–882, jul 2002.

[57] M. Alessandrini, S. Maggio, J. Poree, L. De Marchi, N. Speciale, E. Franceschini, O. Bernard, and O. Basset, "A restoration framework for ultrasonic tissue characterization," *IEEE Trans. Ultrason. Ferroelectr. Freq. Control*, vol. 58, no. 11, pp. 2344–2360, nov 2011.

[58] T. Taxt and J. Strand, "Two-dimensional noise-robust blind deconvolution of ultrasound images," *IEEE Trans. Ultrason. Ferroelectr. Freq. Control*, vol. 48, no. 4, pp. 861–867, 2001.

[59] O. V. Michailovich and D. Adam, "A novel approach to the {2-D} blind deconvolution problem in medical ultrasound," *IEEE Trans. Med. Imaging*, vol. 24, no. 1, pp. 86–104, jan 2005.

[60] R. Chartrand and Wotao Yin, "Iteratively reweighted algorithms for compressive sensing," in *2008 IEEE Int. Conf. Acoust. Speech Signal Process.* IEEE, mar 2008, pp. 3869–3872.

[61] O. Michailovich and Y. Rathi, "Adaptive learning of tissue reflectivity statistics and its application to deconvolution of medical ultrasound scans," in *2015 IEEE Int. Ultrason. Symp.* IEEE, oct 2015, pp. 1–4.

[62] J. A. Fessler and B. P. Sutton, "Nonuniform fast fourier transforms using min-max interpolation," *IEEE Trans. Signal Process.*, vol. 51, no. 2, pp. 560–574, 2003.